

BIGRE: A LOW CROSS-TALK INTEGRAL FIELD UNIT TAILORED FOR EXTRASOLAR PLANETS IMAGING SPECTROSCOPY

JACOPO ANTICHI^{1,2}, KJETIL DOHLEN³, RAFFAELE G. GRATTON², DINO MESA², RICCARDO U. CLAUDI², ENRICO GIRO², ANTHONY BOCCALETTI⁴, DAVID MOUILLET¹, PASCAL PUGET¹, AND JEAN-LUC BEUZIT¹

¹ LAOG-Laboratoire d’Astrophysique de Grenoble, B.P. 53, F-38041 Grenoble Cedex 9, France

² INAF-Osservatorio Astronomico di Padova, Vicolo dell’Osservatorio 5, I-35122 Padova, Italy

³ LAM-Laboratoire d’Astrophysique de Marseille, B.P. 8, F-13376 Marseille Cedex 12, France

⁴ LESIA-Laboratoire d’Etudes Spatiales et d’Instrumentation en Astrophysique, F-92190 Meudon, France

Received 2008 February 11; accepted 2009 January 16; published 2009 April 6

ABSTRACT

Integral field spectroscopy represents a powerful technique for the detection and characterization of extrasolar planets through high-contrast imaging since it allows us to obtain simultaneously a large number of monochromatic images. These can be used to calibrate and then to reduce the impact of speckles, once their chromatic dependence is taken into account. The main concern in designing integral field spectrographs for high-contrast imaging is the impact of the diffraction effects and the noncommon path aberrations together with an efficient use of the detector pixels. We focus our attention on integral field spectrographs based on lenslet arrays, discussing the main features of these designs: the conditions of appropriate spatial and spectral sampling of the resulting spectrograph’s slit functions and their related cross-talk terms when the system works at the diffraction limit. We present a new scheme for the integral field unit based on a dual-lenslet device (BIGRE), that solves some of the problems related to the classical Traitement Intégral des Galaxies par l’Étude de leurs Rays (TIGER) design when used for such applications. We show that BIGRE provides much lower cross-talk signals than TIGER, allowing a more efficient use of the detector pixels and a considerable saving of the overall cost of a lenslet-based integral field spectrograph.

Key words: instrumentation: spectrographs – planetary systems – techniques: high angular resolution – techniques: image processing

Online-only material: color figures

1. INTRODUCTION

Imaging of a significant number of extrasolar planets requires achieving star versus planet contrasts of $\sim 10^6$ (young giant planets), or even 10^8 – 10^{10} (old giant and rocky planets) at a few tenths of an arcsecond from a star, whose value is $\sim 10 \cdot \lambda/D$ in the near infrared for telescopes having pupil sizes of $D \sim 10$ m.

In this regime, the dominant noise contribution is due to the stellar background. To achieve these ambitious goals, high-contrast imagers usually include various components. First, an extreme adaptive optics (XAO) system is used, allowing us to correct aberrations up to a high order, and providing a high Strehl ratio (SR). Second, some coronagraph is included, attenuating the coherent diffraction pattern of the on-axis point-spread function (PSF). Proper combination of these two devices allows reduction of the stellar background down to values of $\sim 10^{-5}$ out to the adaptive optics (AO) system control radius⁵, for a state-of-the-art system. This background is due to a rapidly changing halo of speckles generated by residual telescope pupil phase distortions that have special frequencies close to those of planet images. In order to avoid false alarms, the detection threshold level should then be set at several times the root mean square (rms) noise level.

Even in the favorable case, where the speckle intensity distribution can be assumed to be Gaussian (Marois et al. 2008a), the detection confidence limit should be at least 5 times the noise level. This implies that at angular separations $\leq 10 \cdot \lambda/D$, the limiting contrast provided by state-of-the-art

XAO and coronagraphy is $\sim 2 \times 10^4$ for 8–10 m telescopes. In addition, phase aberrations originating inside the optical train not corrected by the XAO system produce speckles of longer lifetime (minutes or hours) than those due the atmosphere. Other slowly varying (of the order of seconds) phase errors are due to aliasing effects in the wavefront sensor (Poyneer & Macintosh 2004) and—for coronagraphic systems—to adaptive optics time lag (Macintosh et al. 2005).

Beyond a handful of favorable cases where planets are warm, e.g., Chauvin et al. (2004); Chauvin et al. (2005); Neuhaeuser et al. (2005), or with large separation from their parent star (Kalas et al. 2008), or eventually with both these properties (Lafrenière et al. 2008; Marois et al. 2008b), additional techniques are required to reach the larger contrasts needed for extrasolar planets detection.

Simultaneous differential imaging (SDI) is a high-contrast imaging differential technique by which subtraction of different images of the same field acquired simultaneously by the same instrument allows us to remove or reduce the noise produced by atmospheric and instrumental phase aberrations. The SDI principle can be applied to images obtained with different polarization modes (Gisler et al. 2004) or selecting two distinct wavelengths in a fixed spectral range (Lenzen et al. 2005; Marois et al. 2005), or better exploiting the entire spectral range by integral field spectroscopy (Berton et al. 2006). In this paper, we will focus on SDI based upon this latter strategy only.

Essentially, SDI is a calibration technique (Smith 1987; Racine et al. 1999; Marois et al. 2000; Sparks & Ford 2002; Biller et al. 2004; Berton et al. 2006; Ren & Wang 2006; Thatte et al. 2007): images are acquired simultaneously in bands at

⁵ $\propto 1/2d$, $d \equiv$ actuator spacing projected on the telescope pupil.

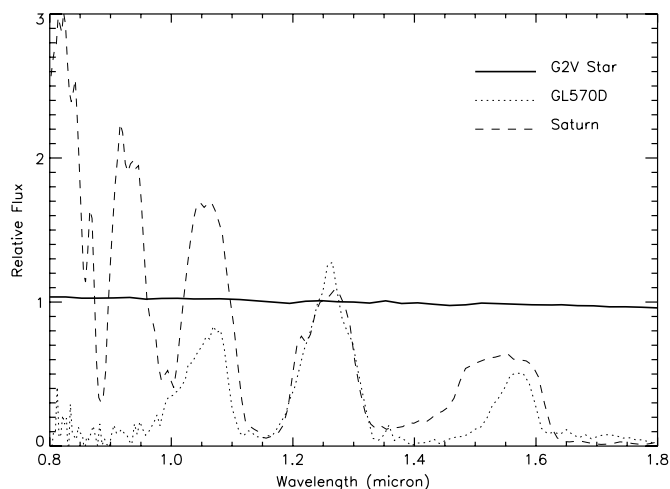


Figure 1. Near-infrared low-resolution spectra (two-pixel resolving power $R = 50$) of the Brown Dwarf GL 570 D of the planet Saturn and of a G2V star (by courtesy of Dr. L. Testi and Dr. F. Ghinassi) obtained at TNG+NICs with its Amici Prism. The spectra are normalized to their flux at $1.30 \mu\text{m}$.

close wavelengths where the planetary (but not the stellar) flux differs appreciably. Subtracting each other these images should allow us to remove or at least reduce the speckle noise, since this is assumed to be similar in the various images after a suitable chromatic rescaling, while the planet signal is left nearly untouched.

There are at least two ways to exploit this calibration technique. In a more traditional approach, specific characteristics of the (expected) planetary spectra are exploited. As indicated by various theoretical work (Sudarsky et al. 2000; Baraffe et al. 2002; Burrows et al. 2003; Sudarsky et al. 2003; Burrows et al. 2004) and observations (e.g., brown dwarfs and gaseous planets in the solar system), the spectra of giant planets are dominated by several absorption bands (mainly due to methane and water vapor) at both visible and near-infrared wavelengths. In such a case, SDI may work by subtracting images where the planet signal is absent from those where it is present, while the background is nearly the same, because the spectrum of the parent star is nearly featureless (see Figure 1). The main advantage of this technique is the minimum assumptions required on the chromatic behavior of speckles; however, this technique allows only a limited reduction of noise. Alternatively, we might try to model the variation of speckles with a wavelength (Sparks & Ford 2002). In principle, this allows us to remove completely speckle noise without making any assumption about the planetary spectrum, hence allowing us to retrieve the real planetary spectrum (Thatte et al. 2007).

Independently of the adopted SDI recipe, integral field spectrograph designs tuned for diffraction-limited high-contrast imaging should take into account several effects, jeopardizing the interpolation procedures requested before simultaneous spectral subtractions, which in turn severely limit the accuracy of this calibration technique.

In this paper, we present a discussion of these effects and derive the basic equations that should be considered when designing lenslet-based diffraction-limited integral field spectrographs. Then, we describe a new concept for the lenslet array, shaping the IFU of such instruments (i.e., BIGRE) and allowing us to improve significantly over the main limitations of the more traditional designs based on the ‘Traitement Intégral des Galaxies par l’Étude de leurs Rays (TIGER) concept.

The structure of the paper is as follows. In Section 2, we recall the basics of a postcoronagraphic speckle field. In Section 3, we summarize the principle of SDI. In Section 4, we discuss the basics of spectroscopic SDI (hereafter S-SDI), defining the conditions allowing us to avoid aliasing errors when sampling both the entrance speckle field and the final exit slit functions. In Section 5, we present various options for IFS instruments suited for S-SDI. In Section 6, we define the cross-talk terms in the case of diffraction-limited lenslet-based IFS. In Section 7, we derive the rules governing the image propagation at the diffraction limit through the TIGER concept, and in Section 8, the ones proper to the new BIGRE concept. Specifically, we explain here how to conceive a BIGRE-oriented IFS instrument adopting standard dioptric devices. In Section 9, we present two design setups (based on BIGRE and TIGER, respectively) for SPHERE,⁶ indicating the solution adopted for its future IFS. In Section 10, we compare the TIGER and the BIGRE concepts in terms of coherent and incoherent signals suppression, considering several cases for the single lens shape and the IFU lattice configuration. Finally, our conclusions are drawn in Section 11.

2. POSTCORONAGRAPHIC SPECKLE FIELD MODELING

An appropriate understanding of chromatic intensity (e.g., Racine et al. 1999) and spatial (e.g., Sparks & Ford 2002) scalings of a speckle field is basic to any application of the SDI calibration technique. For this reason, a short description of these physical concepts is fundamental to introduce the reader to the topics treated in the rest of the paper. Inspired by the approach of Perrin et al. (2003), we will use the Fraunhofer approximation to describe the impact of small residual phase variations of the electric field (e) imaged on a fixed postcoronagraphic entrance pupil plane,⁷ i.e., the working case of high-contrast imaging instruments like SPHERE.

While this approach allows a simple mathematical treatment and physical understanding, it ignores more complex effects due to amplitude errors and Fresnel propagation, as pointed out by Marois et al. (2006). It is outside the scope of this paper to discuss such effects, which can be minimized by careful instrument design, but it is likely that they will set the ultimate limit of planet imaging.

The most general expression of the monochromatic electric field once projected on the coronagraphic entrance pupil plane is

$$e \equiv p \cdot \exp[i \cdot \phi], \quad (1)$$

where (p) is the coronagraphic pupil transmission function, and (ϕ) is the phase of the electric field evaluated over this coronagraphic pupil plane. Assuming a perfect optical propagation from the telescope to this plane—i.e., no differential chromatical aberrations in the beam—the chromatism of the phase can be written explicitly as a function of the wavelength (λ) and the wavefront error (w) as follows:

$$\phi = \frac{2\pi}{\lambda} \cdot w. \quad (2)$$

⁶ SPHERE is an instrument designed and built by a consortium of LAOG, MPIA, LAM, LESIA, LUAN, INAF, Observatoire de Genève, ETH, NOVA, ONERA, and ASTRON in collaboration with and under from ESO. Its science objective is the direct detection and characterization of giant extrasolar planets in the visible and near-infrared (Beuzit et al. 2008).

⁷ Hereafter Fourier pairs are defined with the same letter written in small and capital case respectively.

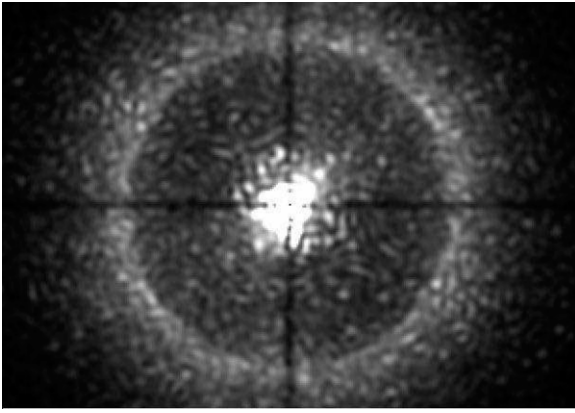


Figure 2. Example of a postcoronagraphic speckle field (integration time = 0.5 ms, wavelength = 1 μm), simulating the XAO system and the four quadrant phase mask coronagraph of SPHERE (by courtesy of the SPHERE team).

Assuming as real the expectation value of the wavefront error given by an XAO system in the near-infrared (i.e., $w \lesssim 10^{-2} \mu\text{m}$ at $\lambda \sim 1 \mu\text{m}$), Equation (1) can be approximated as follows:

$$e = p \cdot (1 + i \cdot \phi). \quad (3)$$

At this point, the action of an unspecified coronagraph can be formalized directly on the coronagraphic exit pupil plane. The goal of the coronagraph is to cancel as much as possible the amplitude of the electric field along the optical axis on this plane. Exploiting Equation (3), the resulting on-axis electric field (e_c) for a perfect coronagraph⁸ is then

$$e_c = e - p = i \cdot p \cdot \phi, \quad (4)$$

or, by Equation (2), is equal to

$$e_c = i \cdot \frac{2\pi}{\lambda} \cdot p \cdot w. \quad (5)$$

Defining finally (E_c , P , W) as the Fourier transforms (FT) of (e_c , p , w), Equation (5) allows us to express the monochromatic postcoronagraphic speckle field (S) as

$$S(\lambda) \equiv |E_c(\lambda)|^2 = \left(\frac{2\pi}{\lambda}\right)^2 \cdot |P \otimes W|^2. \quad (6)$$

Equation (6) shows that the intensity of a speckle field scales proportionally to λ^{-2} , while its chromatic wavelength scaling comes from the fact that the variable involved in the wavefront w is the spatial frequency (ν) and not the position (x) in the image plane, i.e.,

$$w(\nu) \equiv \text{FT}[W(x)]. \quad (7)$$

This indicates that spatial frequency translates into position according to wavelength, e.g., by applying the standard grating equation as follows:

$$m \cdot \lambda = g \cdot \sin(\theta), \quad (8)$$

⁸ A perfect coronagraph removes actually the coherent part of the electric field amplitude due to the on-axis optical beam only, see e.g., Cavarroc et al. (2006); here, we consider the total amplitude in order to simplify the related formalism.

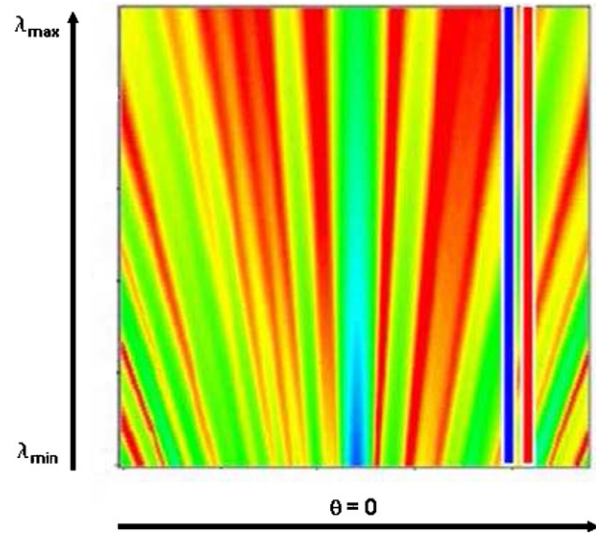


Figure 3. Cuts through the data cube obtained by the chromatical dispersion of a postcoronagraphic speckle pattern resulting from end-to-end simulations of the IFS inside SPHERE (intensity increases from red to blue colors). Position on sky (θ) is on the horizontal axis, while the spectral range (λ_{\min} – λ_{\max}) is on the vertical axis. The red and blue lines indicate two spectra taken at different radial distances to the optical axis. Moving along these spectra, a variable pseudo-periodic modulation due to the speckle chromatism is clearly visible (by courtesy of the SPHERE team).

(A color version of this figure is available in the online journal.)

where m is the diffraction order, θ is the diffraction angle, and g is the grating constant corresponding to the spatial frequency (ν), or,

$$g(\nu) \equiv \left(\frac{1}{\nu}\right), \quad (9)$$

the position on the image plane returns

$$x = f \cdot \sin(\theta), \quad (10)$$

with f being the focal length of the postcoronagraphic reimaging optics. Using Equations (8) and (9), this position can be written finally as

$$x = f \cdot m \cdot \lambda \cdot \nu. \quad (11)$$

Equation (11) indicates that the position of a speckle corresponding to a given fixed spatial frequency due to the postcoronagraphic wavefront error scales linearly with wavelength (Sparks & Ford 2002). More in detail, this means that for every fixed position in the image plane, speckles corresponding to distinct spatial frequencies get distinct wavelengths (Figure 3). We call this feature speckle chromatism.

3. THE SDI CALIBRATION TECHNIQUE FRAMEWORK

In the approach considered in this paper, the fundamental SDI step is the simultaneous acquisition of images at adjacent wavelengths in a spectral range where the planetary and stellar spectra differ appreciably. From ground-based observations, the wavelength bands Y , J , H , and K are well suited for extrasolar giant planets (Beuzit et al. 2008; Macintosh et al. 2008), and rocky planets (Vérinaud et al. 2008).

Let $S(\lambda, \theta)$ be the monochromatic spectral signal corresponding to a fixed angular position (θ) on sky expressed as the sum of the spectral signal of the star, $S_t(\lambda, \theta)$, and the spectral signal of a candidate low-mass companion (e.g., an extrasolar planet)

which lies specifically in this angular position, $PI(\lambda, \theta)$. Fixing a pair of wavelengths (λ_1, λ_2) inside the window above, the following relations hold:

$$S(\lambda_1, \theta) = St(\lambda_1, \theta) + PI(\lambda_1, \theta) \quad (12)$$

$$S(\lambda_2, \theta) = St(\lambda_2, \theta) + PI(\lambda_2, \theta). \quad (13)$$

The basic SDI assumption is that after suitable flux normalization and chromatic rescaling, the following relations hold for the boundary wavelengths of the range above:

$$St(\lambda_1, \theta) = St(\lambda_2, \theta) \quad (14)$$

$$PI(\lambda_2, \theta) = 0. \quad (15)$$

Then the difference between $S(\lambda_1, \theta)$ and $S(\lambda_2, \theta)$ should return—in principle—the spectral signal $PI(\lambda_1, \theta)$ only, i.e., the one appropriate to the low-mass (or extrasolar planet) candidate. However, while working with narrow-band filters several precautions are required.

1. An image taken with one filter has to be spatially rescaled before confronting it with a second image taken with a different filter due to the speckle scaling described in Section 2;
2. Any filter separating two adjacent spectral bands should have similar spectral transmission profiles;
3. The difference ($\delta\lambda_{ij}$) between the central wavelengths (λ_i, λ_j) of two adjacent filters should be as small as possible.

The last point is the most critical due to the fact that chromatism of the speckle field always induces a certain amount of phase errors. Adopting the formalism of Marois et al. (2000), the residual wavefront distortion can be described through the Fourier transform of the postcoronagraphic wavefront error (W), or by its relative chromatic phase error (Φ).

Adopting the standard approximation for the SR (Maréchal 1947), it is possible to transfer this rms wavefront error (σ_Φ) on a relative flux variation on the detector plane. In detail, defining $\sigma_\Phi(\lambda)$ as the rms chromatic wavefront error, Marois et al. (2000) found the following relation for the flux residual between images taken with two narrow-band filters (i, j):

$$\frac{\Delta S_{i,j}}{S_{i,j}} = 2 \cdot \sigma_\Phi^2(\lambda_i) \cdot \frac{\delta\lambda_{i,j}}{\lambda_i}. \quad (16)$$

Equation (16) indicates that with the so-called *single difference* method, the final error is proportional to

1. the variance of the wavefront error: σ_Φ^2 ,
2. the relative wavelength separation between the narrow-band filters: $\delta\lambda_{i,j}/\lambda_i$.

The need for a calibration technique more efficient than SDI but still based on the simultaneous difference of chromatic images of the same target field was addressed theoretically by Marois et al. (2000), which showed that the speckle noise reduction could be much more efficient if observations at three wavelengths were available using their *double difference* method, and verified experimentally with the discovery of the first planet by using this calibration technique (Lagrange et al. 2008).

Starting from there, it is reasonable to assume that a larger number of images at different wavelengths, taken with a regular

spectral step, can result in even better reduction of speckle noise with a true S-SDI calibration technique. The gain could be even larger if observations at several wavelengths would allow an accurate derivation of the chromatic wavelength scaling, as proposed by, e.g., Thatte et al. (2007). This thought suggests the use of integral field spectroscopy for collecting data simultaneously at a large number of wavelengths given by the total spectral length and the spectral resolution of a suitable disperser (Berton et al. 2006).

Note that such an approach is convenient even in the more conservative approach where modeling of the spectral dependence fails, simply because a larger number of wavelength pairs can be constructed.

4. THE S-SDI CALIBRATION TECHNIQUE FRAMEWORK

Exploiting an IFU as field stop array over an optical plane conjugated with the focal plane of the telescope itself allows an appropriate sampling of the postcoronagraphic speckle field defined by Equation (6). The fact that this optical signal gets a finite cut-off spatial frequency proportional to D/λ_{\min} , where D is the postcoronagraphic pupil size, and λ_{\min} is the spectrograph's cut-on wavelength, means that a correct spatial sampling on this plane should be imposed searching for suitable sizes for the separation between adjacent spaxels,⁹ which in turn compose the adopted IFU. This sampling condition is detailed in Section 4.1.

The request of a sampling criterion based upon the Shannon theorem is mandatory not only at the level of the IFU spaxels but also at the level of the detector pixels. In this case, the Shannon sampling condition allows us to interpolate correctly, both spatially and spectrally, the exit slit functions, which in turn are the final output of an integral field spectrograph. These two sampling conditions are detailed in Sections 4.2 and 4.3, respectively.

4.1. Spatial Sampling of the Entrance Speckle Field

Let F_{in} be the focal ratio by which the postcoronagraphic speckle field is projected on the IFU plane. Theory of image formation (e.g., Goodman 1996) implies then that the cut-off spatial frequency appropriate to S can be written as a function of F_{in} and λ_{\min} as follows:

$$\nu_C = \left(\frac{1}{F_{\text{in}} \cdot \lambda_{\min}} \right). \quad (17)$$

The spaxel size (D_{spaxel}) defines the Nyquist spatial frequency on this plane:

$$\nu_{\text{Ny}} \equiv \left(\frac{1}{2 \cdot D_{\text{spaxel}}} \right). \quad (18)$$

Thus, the Shannon sampling theorem applied to the IFU plane returns:

$$\nu_{\text{Ny}} \geq \nu_C. \quad (19)$$

4.2. Spatial Sampling of the Spectrograph's Exit Slits

The condition avoids aliasing effects when interpolating the array of exit slits over the whole range of wavelengths considered by the spectrograph, and it may be written through the following formalism.

⁹ Spaxel indicates a spatial pixel appropriate to the IFU subsystem inside an IFS instrument. An IFU in turn is the matrix of spaxels which should be placed on the reimaged telescope focal plane, working as an optical field-stop array.

The detector pixel size (d_{pixel}) defines the Nyquist spatial frequency on this plane:

$$\mu_{\text{Ny}} \equiv \left(\frac{1}{2 \cdot d_{\text{pixel}}} \right). \quad (20)$$

Once the final spectrograph's exit slits are imaged on the detector pixels through a fixed output focal ratio (F_{out}) and an optical magnification (m_{IFS}), theory of image formation, e.g., Goodman (1996), implies that their spatial cut-off frequency is

$$\mu_{\text{C}} = \left(\frac{1}{\lambda_{\text{min}} \cdot m_{\text{IFS}} \cdot F_{\text{out}}} \right), \quad (21)$$

where λ_{min} indicates the shortest wavelength imaged by the spectrograph. We define the supersampling condition as

$$\mu_{\text{Ny}} \geq \mu_{\text{C}}. \quad (22)$$

4.3. Spectral Sampling of the Speckle Field Over the Entire Field of View

When working with a speckle pattern data cube, chromatic resampling is needed to obtain both monochromatic images, as indicated by Marois et al. (2000), or spectra, as indicated by Thatte et al. (2007).

To this aim, Sparks & Ford (2002) suggested to adopt a suitable pixel-dependent resampling of the speckle field which varies according to wavelengths, while Ren & Wang (2006) developed a subtraction algorithm based upon analytical modelings of the spectral content of a speckle field. Anyhow, before any resampling recipe, it is important to find out the exact condition allowing us to avoid aliasing errors due to the speckle chromatism effect.

Since the speckle pattern scales proportionally to wavelength (Section 2), a feature located at an angular distance θ from the central star at wavelength λ moves spectrally at a rate of $d\lambda/d\theta = \lambda/\theta$. Spatial speckles of width $\delta\theta_s = \lambda/D$, therefore, translates into spectral speckles of width

$$\delta\lambda_s = \frac{\lambda^2}{\theta \cdot D}, \quad (23)$$

i.e., the spectral extension of speckles is inversely proportional to the distance from the field center. Nyquist sampling of spectral speckles requires spectral sampling ($\delta\lambda_p$) corresponding to half the speckle width, so far a two-pixel resolving power ($R = \lambda/2\delta\lambda_p$), Nyquist sampling implies the following condition:

$$R > \frac{\lambda}{\delta\lambda_s} = \theta \cdot \frac{D}{\lambda}. \quad (24)$$

This condition will be fulfilled within a field angle θ_{Ny} , referred to as the Nyquist radius, given by

$$\theta_{\text{Ny}} = R \cdot \frac{\lambda}{D}. \quad (25)$$

We note that it is possible to ensure Nyquist sampling in a system which does not fulfill the supersampling condition written in Equation (22), as long as its field of view does not exceed the Nyquist radius and as long as the source itself does not contain spectral features which violate the Shannon theorem.

For example, an instrument operating on an 8 m telescope at $1.6 \mu\text{m}$ with a full field of view of 5 arcsec, would require a two-pixel resolving power of at least 60. For systems where larger field of view or lower resolving power is required, the supersampling condition must be fulfilled. In these systems, the zone lying within the Nyquist radius fulfils both Equations (22) and (24). We refer to this double fulfillment as hypersampling.

For an integral field spectrograph covering a spectral range fixed between a cut-on (λ_{min}) and a cut-off wavelength (λ_{max}), where λ_c represents the central one, the hypersampling condition will be valid over the whole spectral range within the radius

$$\theta_{\text{Ny}} = \frac{\lambda_{\text{min}}^2 \cdot R}{D \cdot \lambda_c}. \quad (26)$$

5. OPTIONS FOR THE IFS CONCEPT REALIZING S-SDI

IFS needs a very large number of pixels at the level of the final image plane where the matrix of spectra is acquired by the detector. This issue is particularly important when spectral and spatial information are recorded simultaneously in the detector plane, such as for IFS based on the image slicer or the TIGER¹⁰ concepts.

The image slicer option is more efficient in terms of detector pixels usage, since no separation between spectra from adjacent pixels is required in one space dimension. Assuming a square detector, the number of detector pixels (N_{det}^2) required for a given number of spaxels (N_{spaxel}^2) and the number of spectral samples (N_{spec}) are given by the following relation:

$$N_{\text{det}}^2 = N_{\text{spaxel}}^2 \cdot N_{\text{spec}}. \quad (27)$$

In this concept, a bidimensional field of view is divided by mirrors into strips, and then reformatted on a mono-dimensional pseudo-long slit (see e.g., Prieto & Vives 2006, Figure 1). Monochromatic exit slits will be then obtained downstream by using a standard collimator, disperser, and camera optical system. A potential problem of the image slicer design concerns the noncommon path aberrations in adjacent spaxels of the field of view that fall on different slices. However, this concept has been proved able to obtain (moderately) high-contrast images from ground even without coronagraphic devices and with moderate SRs (~ 0.3 – 0.5 ; Thatte et al. 2007). A further examination of an image slicer instrument dedicated to high-contrast diffraction-limited imaging spectroscopy is on progress within the feasible study for the future E-ELT Planet Finder facility (Kasper et al. 2008).

On the other hand, noncommon path aberrations are expected to be very small in the case of the TIGER-type concept (Bacon et al. 1995), which uses an IFU based on a matrix of lenses with fixed lens pitch. In this case, spectra given by individual spaxels should be separated on the detector. For a separation of N_{sep} between spectral samples, the required number of detector pixels becomes

$$N_{\text{det}}^2 = N_{\text{spaxel}}^2 \cdot N_{\text{spec}} \cdot N_{\text{sep}}. \quad (28)$$

The lenslet-based concept then requires a large number of detector pixels. However, the format of image slicer IFS data on the detector is suited for spectra with many spectral elements,

¹⁰ "TIGER" is a French acronym standing for "Traitement Intégral des Galaxies par l'Étude de leurs Rays," has Bacon et al. (1995) named their lenslet-based IFS.

i.e., $> 10^2$, and a relatively small number of spaxels, i.e., $< 10^4$. These are not typical values for instruments dedicated to planet search that generally requires short spectra (~ 20 – 30 spectral elements) for a large number of spaxels ($\sim 10^5$). In order to adequately exploit the detector, the number of slices should be roughly given by the ratio between the spaxels and the length of the spectra. This value is $\sim 10^3$ for an integral field spectrograph tuned to planet finding, which would result in an extremely long pseudoslit. The format of the image slicer IFU then exacerbates the problems related to noncommon paths: photons from adjacent spaxels may have very different paths through the instrument. It is then difficult to maintain small phase errors, possibly compromising most demanding high-contrast imaging.

Given the difficulties inherent to the image slicer solution, we carefully examined the properties of the lenslet-based design, trying to minimize the separation between spectral samples. To this aim, we developed the new optical concept proposed by Dohlen et al. (2006): BIGRE.¹¹ The properties of this design are discussed and compared to the TIGER ones, starting from Section 8.

6. INCOHERENT AND COHERENT CROSS TALKS OF A LENSLET-BASED IFU

Adopting the formalism of Goodman (1996), any spaxel of an IFU is a sum of linear optical systems. In the specific case of a lenslet-based IFU, these systems are single lenses. The coherent and incoherent parts of the electric field incoming onto these optical linear systems are transmitted in a different way through two adjacent spaxels. Specifically, when the illumination is coherent, the linear responses of adjacent spaxels vary in unison, and therefore their signals, once transmitted and reimaged on the spectrograph's slits plane, must be added in complex amplitude. In contrast, when the illumination is incoherent, the linear responses of two adjacent spaxels are statistically independent. This means that their signals, once transmitted and reimaged on the spectrograph's slit plane, must be added in intensity.

Hence, once dispersed and reimaged by the spectrograph's optics,¹² monochromatic slits corresponding to adjacent spaxels will suffer from a certain amount of interference. We call this quantity coherent cross talk. Furthermore, monochromatic slits will be affected by a spurious amount of signal due to its adjacent spectra. We call this quantity incoherent cross talk. With reference to Figure 4, coherent cross talk is the interference signal between monochromatic spectrograph's entrance slits which correspond to adjacent lenses, i.e., separated by a distance equal to the IFU lens pitch,¹³ while incoherent cross talk is the spurious signal registered over a fixed monochromatic spectrograph's exit slit and due to its closest spectra, even if due to photons of different wavelength.

Incoherent and coherent cross talks represent a major issue identifying the best solution for the spaxels shape (circular, square, etc.), the lenslet lattice configuration (hexagonal, square,

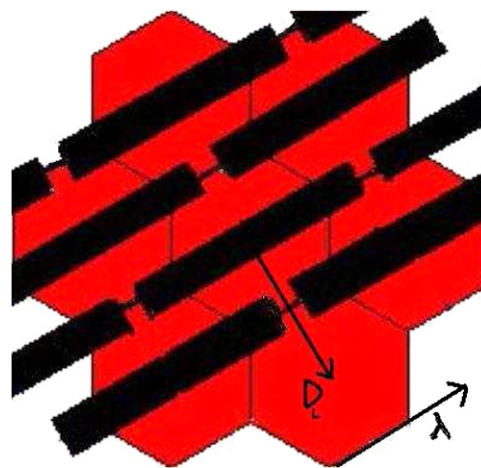


Figure 4. Sketch of the final spectra (black rectangles) superimposed on an array of seven (red) hexagonal spaxels, down of a lenslet-based IFU. D_L indicates the IFU lens pitch, while the dispersion axis is indicated through a black arrow labeled with the symbol λ .

(A color version of this figure is available in the online journal.)

etc.), and for the geometric allocation of the spectra at the level of the detector plane. In fact, incoherent and coherent cross talks are spurious signals—not removed by the application of supersampling and hypersampling criteria—which still affect the final array of spectra, thus damaging the final three-dimensional data cube. The selection of the kind of field unit to be mounted at the entrance of a lenslet-based integral field spectrograph should then depend on the estimate of the level of incoherent and coherent signals over the individual exit slits of such a spectrograph. Additional considerations should enter in this choice, e.g., the fact that the relevance of the cross-talk terms depends on the wavefront errors after the coronagraph or that minimization of the cross talk might result in a system design which is potentially less efficient when observations are limited by photon noise. In general, cross talk should be specified so that its contribution to the contrast error budget is less than the flat field errors and all remaining spurious effects affecting the postcoronagraphic speckle field.

6.1. Coherent Cross Talk: The Formalism

Basically, coherent cross talk is the interference of a beam passing through a number of apertures (individual lenslets) and measured on a screen (the spectrograph's entrance slits plane) conjugated to the detector plane.

Let us assume a flat wavefront impinging onto the IFU lenses. Let now E_1 be the complex electric field of the coherent signal transmitted by spaxel 1 on the spectrograph's entrance slits plane. Let dE_2 be the stray part of the complex electric field of the coherent signal transmitted by spaxel 2 (spaxel 2 being adjacent to spaxel 1) and evaluated in the position of the slit corresponding to spaxel 1. E_1 and dE_2 are complex quantities that differ according to the phase difference, which is due to different optical paths through different apertures (lenslets). The effective coherent intensity measured on the spectrograph's entrance slits plane and corresponding to the position of spaxel 1 will then be

$$I_1^C \equiv |E_1 + dE_2|^2. \quad (29)$$

In the worst case, the phase difference of waves passing through adjacent lenses is πk ($k \in \mathbb{Z}$). In this case and neglecting the term $|dE_2|^2$ in the binomial expression of Equation (29), the

¹¹ “BIGRE” was the first word uttered by G. Courtes—the inventor of the TIGER concept—while the authors explained him all the problems of diffraction-limited IFS and their possible resolution using this new optical concept. “BIGRE” is a French exclamation with a meaning similar to the British: “Bligh-me” or the Italian: “Accidenti.”

¹² The dispersion axis can be defined orienting the spectrograph's disperser with respect to a reference frame fixed on to the IFU.

¹³ The pitch of an array of spaxels is defined as the center-to-center distance among adjacent ones. For a filling factor close to unity, this quantity equals the size of the single spaxel.

effective coherent intensity proper to spaxel 1 becomes

$$I_1^C = I_1 + 2 \cdot |E_1| \cdot |dE_2| = I_1 \cdot (1 + \text{CCT}). \quad (30)$$

CCT is defined as the coherent cross-talk coefficient:

$$\text{CCT} \equiv 2 \cdot \frac{|dE_2|}{|E_1|} = 2 \cdot \left(\frac{dI}{I_1} \right)^{1/2}, \quad (31)$$

where the stray coherent intensity proper to spaxel 2 evaluated in the position of spaxel 1 is defined as

$$dI \equiv |dE_2|^2, \quad (32)$$

and the own coherent intensity of spaxel 1 is defined as

$$I_1 \equiv |E_1|^2. \quad (33)$$

CCT represents the maximum extra amount of coherent signal on the slit function corresponding to a fixed lenslet aperture, and its estimate can be given by measuring the square root of the coherent intensity proper to the slit function corresponding to the adjacent aperture. However, the total amount of coherent cross talk is obtained only by adding the contribution due to all the apertures in the lenslet array.

6.2. Incoherent Cross Talk: The Formalism

The amount of spurious incoherent light can be evaluated directly on the detector plane, where a single exit slit appears as a spectrum. As indicated in Figure 4, any final spectrum is surrounded by several adjacent spectra.

Let $I_1(\lambda)$ be the intensity proper to a fixed monochromatic exit slit; due to the presence of an adjacent exit slit its effective incoherent intensity will be

$$I_1^{INC}(\lambda) \equiv I_1(\lambda) + dI_2(\lambda), \quad (34)$$

where $dI_2(\lambda)$ is the stray incoherent monochromatic intensity of a given adjacent exit slit, evaluated at a distance equal to the separation to the fixed one

$$dI_2(\lambda) \equiv \text{ICT}(\lambda) \cdot I_1(\lambda), \quad (35)$$

where $\text{ICT}(\lambda)$ is defined as the monochromatic term of the incoherent cross-talk coefficient (ICT).

The incoherent cross-talk coefficient corresponding to the spectrograph's wavelengths range ($\lambda_{\min} - \lambda_{\max}$) is then defined as

$$\text{ICT} \equiv \int_{\lambda_{\min}}^{\lambda_{\max}} \left(\frac{I_1^{INC}(\lambda) - I_1(\lambda)}{I_1(\lambda)} \right) d\lambda. \quad (36)$$

Thus—differently to the coherent case—the incoherent cross talk must be considered on the detector plane, searching for spectral alignments for which the distance among adjacent spectra is minimized. Once this spectral alignment is found, an estimate of ICT can be given by measuring the incoherent intensity of a single monochromatic exit slit at the distance equal to the transversal separation among adjacent spectra. However, the total amount of incoherent cross talk is obtained only by adding the contribution of all the spectra imaged onto the detector plane.

7. DIFFRACTION-LIMITED INTEGRAL FIELD SPECTROSCOPY WITH THE TIGER CONCEPT

In classical TIGER design optimized for seeing limited conditions, the spaxels (or microlenses) comprising the IFU are much bigger than the Airy disk, providing therefore resolved images of the telescope entrance pupil, which in turn represent the entrance slits of this kind of integral field instrument; see e.g., Bacon et al. (1995, 2001).

Differently, in the case of high-contrast imaging the microlenses sample the telescope image according to the Shannon theorem. Each microlens acts like a diaphragm isolating a portion of the incoming electric field and concentrates it into a micropupil image in the focal plane of the microlens, acting as the entrance slit function of the spectrograph. The micropupil image is the convolution between the geometrical pupil image and the PSF of the microlens. As seen below, Nyquist sampling of the focal plane implies that the telescope entrance pupil is unresolved by the microlens.

For a circular lens of diameter D_{spaxel} , the transmission function is $\Pi(u/D_{\text{spaxel}})$, where u is the image co-ordinate normalized to the lens diameter, and $\Pi(x)$ is a top-hat function with unitary transmission within the unitary diameter and zero outside this diameter. According to Equation (19), the size of the single microlens should be

$$D_{\text{spaxel}} \leq \left(\frac{F_{\text{in}} \cdot \lambda_{\min}}{2} \right). \quad (37)$$

Following Born & Wolf (1965), the monochromatic full width at half-maximum (FWHM) of the PSF proper to a circular microlens with focal length f_{out} is

$$\text{FWHM} = f_{\text{out}} \cdot 1.02 \cdot \frac{\lambda}{D_{\text{spaxel}}}, \quad (38)$$

while the geometrical diameter of the micropupil is

$$D_{\text{MPG}} = \frac{f_{\text{out}}}{F_{\text{in}}}. \quad (39)$$

Combining Equations (37), (38), and (39), we obtain

$$\text{FWHM} = 2.04 \cdot \left(\frac{D_{\text{MPG}} \cdot \lambda}{\lambda_{\min}} \right). \quad (40)$$

This size is therefore at least twice as wide as the geometrical pupil, and so the convolution product is approximately equal to the microlens PSF.

Thus, we can say that the field distribution onto the spectrograph's slit plane approximates the one proper to an unresolved micropupil, which is described by the Jinc function¹⁴ corresponding to the microlens aperture:

$$e_{\text{pupil}}(s) \sim \text{Jinc}(s), \quad (41)$$

with s being defined as the pupil the co-ordinate normalized to $\lambda \cdot F_{\text{out}}$, where F_{out} is

$$F_{\text{out}} \equiv \frac{f_{\text{out}}}{D_{\text{spaxel}}}. \quad (42)$$

Finally, the slit function will be the square modulus of the signal

$$\text{SF}(s) = |e_{\text{pupil}}(s)|^2; \quad (43)$$

see Figure 5.

¹⁴ We define Jinc function as the Fourier transform of circular aperture: $\text{Jinc}(x) = (2 \cdot J_1(\pi \cdot x)) / (\pi \cdot x)$, where J_1 indicates the Bessel-J function of order one.

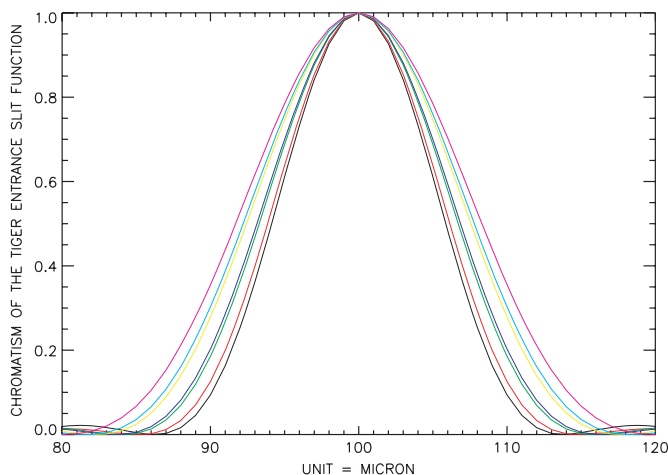


Figure 5. Normalized TIGER entrance slit function. The example shows the case of the IFU optimized for SPHERE in the working wavelengths range: 0.95–1.35 μm ; colors indicate seven distinct wavelengths.

(A color version of this figure is available in the online journal.)

Table 1
Independent Parameters of a TIGER-oriented IFS

Parameter	Symbol
Postcoronagraphic Pupil Size	$\equiv D$
IFS Cut-on Wavelength	$\equiv \lambda_{\min}$
Size of the Single TIGER Microlens	$\equiv D_{\text{spaxel}}$
Focal Length of the TIGER Microlens	$\equiv f_{\text{out}}$
IFS Detector Pixel Size	$\equiv d_{\text{pixel}}$
IFS Optical Magnification	$\equiv m_{\text{IFS}}$
IFS Disperser (two-pixel) Resolving Power	$\equiv R$

7.1. Sampling Analysis Applied to the TIGER Concept

As indicated by Equation (43), the single spectrograph's slit is an unbound signal whose size varies linearly with wavelength. The final pixel size defines the spatial Nyquist frequency on the spectrograph image plane according to Equation (20). Due to its unbound nature, the spatial cut-off frequency of the spectrograph's exit slit gets the finite value fixed by Equation (21). Then, following Equation (22), supersampling imposes a lower limit to the output focal ratio by which the single microlens generates its corresponding micropupil:

$$F_{\text{out}} \geq \left(\frac{2 \cdot d_{\text{pixel}}}{\lambda_{\min} \cdot m_{\text{IFS}}} \right). \quad (44)$$

Output focal ratios lower than the one fixed by Equation (44) introduce aliasing errors in the sampled spectrum, unless the field is smaller than the Nyquist radius. According to Equation (26), the latter depends on the postcoronagraphic pupil size, the spectrograph's working wavelengths range and its spectral resolution. Hence, the true hypersampling is obtained when this radius matches with the maximum image field radius, which in turn is related to the spectrograph's resolving power. Then, for a fixed resolving power, hypersampling is then a matter of allocation of the array of final spectra onto the detector pixels, which in turn depends on the accepted cross-talk levels.

8. DIFFRACTION-LIMITED INTEGRAL FIELD SPECTROSCOPY WITH THE BIGRE CONCEPT

Cross talk in diffraction-limited TIGER-oriented IFU is generally quite large, because the output slit functions, taking

the form of an Airy pattern, decrease slowly with the distance from the center. Suitable apodization of the microlenses might, in principle, be used to reduce the cross-talk terms, but the feasibility of such a scheme remains to be demonstrated. We consider instead an alternative lenslet-based optical scheme that we call BIGRE, which we consider to be much more practical.

As in the TIGER case, the BIGRE spaxel consists of a microlens which acts essentially as a diaphragm isolating a portion of the incident electric field. This lens, of focal length f_1 , focalizes the field into an unresolved micropupil with a field distribution described by Equation (41). Different to the TIGER case, we place a second microlens at a distance equal to its focal length f_2 , behind the micropupil. This lens collects field and reproduces an image of the first lens, behind the micropupil. When $f_2 < f_1$, the final image is reduced, resulting in the same flux-concentrating effect as in the original TIGER concept, but without the field-pupil inversion. We define K factor as the spaxel demagnification factor:

$$K \equiv \frac{f_1}{f_2}. \quad (45)$$

Ideally, for infinitely wide optics throughout the following spectrograph, the slit function is a perfectly bound top-hat function, so no cross talk would be present between spaxels. Of course, this is not physical, and the following finite sized optics modifies the slit function as we will see in the following.

It may also be argued that a perfect top-hat function is not the ideal slit function from a sampling point of view, since its modulus transfer function (MTF) will be unbound and create some aliasing. As we will see, the implementation of a diaphragm of appropriate size modifies the slit function in a way which turns out to be beneficial both from a cross talk and from a sampling points of view.

Figure 6 shows the BIGRE spaxel conceptually, indicating its dimensions and the geometrical ray paths. The two lenslet arrays are implemented as the two surfaces of a single component and the micropupil array occurs within the component. In principle, it would be possible to implement a mask in this micropupil image, but this option has not been retained in view of complexity of manufacturing and aligning a system of three micro-optical elements (lens, diaphragm, lens). Instead, we consider the second lens and the subsequent collimation optics to be sufficiently large to not significantly modify the field transmission, implementing the mask in the metapupil image formed onto the spectrograph's dispersion element (see Figure 10).

While the geometrical micropupil size is given by the focal ratio of the input beam according to Equation (39), the characteristic size of the diffractive micropupil is

$$D_{\text{MP}} = \lambda \cdot \frac{f_1}{D_{\text{spaxel}}}. \quad (46)$$

In the following, we use a pupil co-ordinate unit, s , which is normalized to D_{MP} , allowing us to discuss the size of the pupil diaphragm without worrying about the optical design characteristics of the intervening optics. For the above assumption concerning relatively undisturbed propagation of the electric field from the micropupils to the spectrograph pupil, we need to ensure that the diffracted beam does not get truncated by the second microlens edge. For this, a criterion would be to make sure that the diffractive micropupil is much smaller than the spaxel diameter: $D_{\text{MP}} \ll D_{\text{spaxel}}$. Plugging this condition

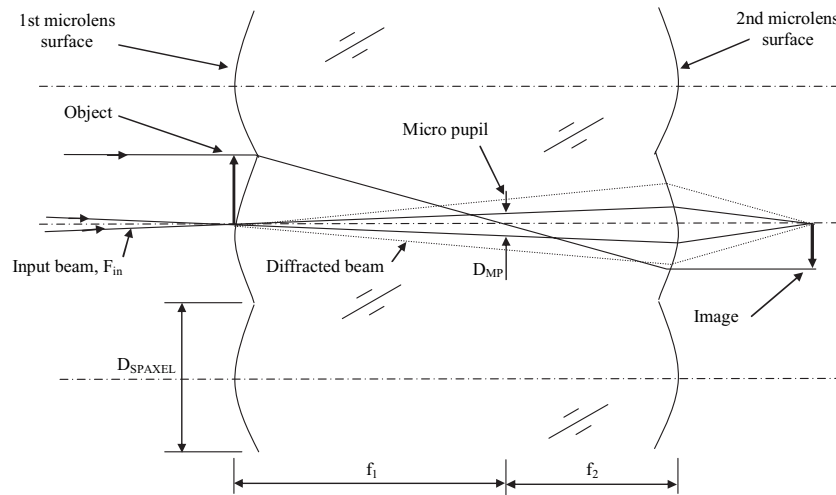


Figure 6. Scheme of a BIGRE spaxel working at the diffraction limit with an un-resolved entrance pupil. The first lens lies on a focal plane and reimages a micropupil at its focal distance (f_1). The electric field imaged onto this optical plane is a sinc function (one dimension) or a Jinc function (two dimensions). This signal is filtered by a top-hat transmission function and finally reimaged onto an image plane by the second lens. The distance between this intermediate pupil plane and the second lens is its focal length (f_2). The electric field imaged by this second lens is an un-bound signal with upper envelope much steeper than the one proper to a sinc profile ($\propto u^{-1}$) or a Jinc profile ($\propto u^{-1.5}$).

into Equation (46), we get the following condition on the focal length of the first surface:

$$f_1 \ll \frac{D_{\text{spaxel}}^2}{\lambda}. \tag{47}$$

Introducing a pupil mask defined by

$$\text{PM}(s) \equiv \Pi(s/S_{\text{PM}}), \tag{48}$$

where $\Pi(x)$ is a top-hat function with unitary transmission within the diameter S_{PM} , which is turn is the pupil mask size in units of s . We can express the electric field distribution in the exit slit plane as

$$E_{\text{slit}}(u) = \text{FT}[e_{\text{pupil}}(s) \cdot \text{PM}(s)]. \tag{49}$$

Hence, evoking the convolution theorem and remembering that the field in the pupil plane is the Fourier transform of the field in the spaxel, this can be rewritten as

$$E_{\text{slit}}(u) = \Pi(u/D_{\text{spaxel}}) \otimes \text{FT}[\Pi(s/S_{\text{PM}})], \tag{50}$$

i.e., the convolution between a top-hat function corresponding to the original spaxel transmission function and a Jinc function corresponding to the micropupil mask.

Finally, the slit function is the square modulus of this signal:

$$\text{SF}(u) = |E_{\text{slit}}(u)|^2, \tag{51}$$

and its spectral modulation transfer function is

$$\text{MFT}(s) \equiv |\text{FT}[\text{SF}(u)]|. \tag{52}$$

8.1. Sampling Analysis Applied to the BIGRE Concept

According to Equation (19), the input focal ratio of the light coming to the single BIGRE spaxel should be

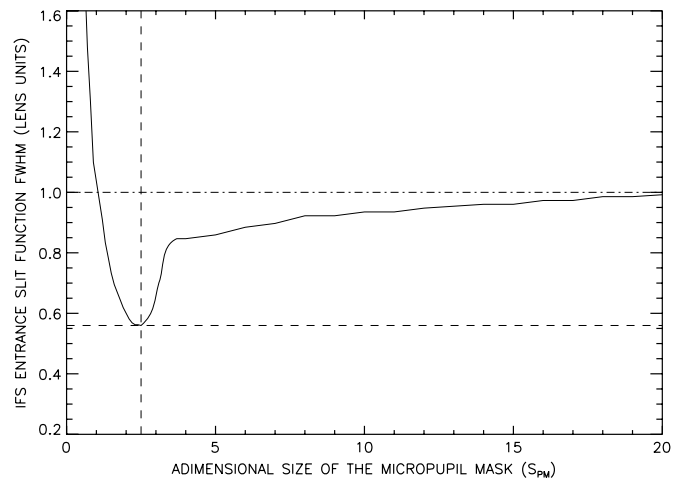


Figure 7. FWHM of the BIGRE entrance slit function profile as a function of the pupil mask size S_{PM} . This FWHM gets its absolute minimum when $S_{\text{PM}} = 2.5$. Dot-dashed horizontal line indicates the asymptotic trend of the FWHM, corresponding to the pupil mask sizes towards the limit: $S_{\text{PM}} = \infty$. Dashed horizontal line indicates FWHM value corresponding to the absolute minimum $S_{\text{PM}} = 2.5$, this one traced with a dashed vertical line.

$$F_{\text{in}} \geq \left(\frac{2 \cdot D_{\text{spaxel}}}{\lambda_{\text{min}}} \right). \tag{53}$$

From the paraxial perspective, input and output focal ratios of a BIGRE spaxel are related to the K factor as follows:

$$F_{\text{out}}^G = \frac{F_{\text{in}}}{K}, \tag{54}$$

and the geometric micropupil size returns

$$D_{\text{MPG}} \equiv \frac{f_1}{F_{\text{in}}}. \tag{55}$$

From the diffractive perspective, the output focal ratio is fixed only when the size of the pupil mask is fixed on the micropupil plane, due to the unbound nature of this micropupil profile. The

characteristic size of the diffractive micropupil (D_{MP}) can be parameterized in terms of the focal ratio of the first BIGRE lens (F_1) and the spectrograph central wavelength (λ_c) as follows:

$$D_{MP} = S_{PM} \cdot \lambda_c \cdot F_1. \quad (56)$$

The diffractive output focal ratio (F_{out}) results then from the following equation:

$$F_{out} = F_{out}^G \cdot \frac{D_{MPG}}{D_{MP}}, \quad (57)$$

or, exploiting Equations (54), (55), and (56):

$$F_{out} = \left(\frac{D_{spaxel}}{K \cdot S_{PM} \cdot \lambda_c} \right). \quad (58)$$

Finally, by Equations (21) and (58), the spatial cut-off frequency of the spectrograph's exit slit becomes

$$\mu_C = \left(\frac{K \cdot S_{PM}}{D_{spaxel} \cdot m_{IFS}} \right). \quad (59)$$

Equation (59) indicates that the actual profile of the spectrograph's slit function is no longer a bound signal, just because the pupil mask gets a finite size. The actual size of the final exit slit function will be then an unbound signal with spatial cut-off frequency depending both on the size of this pupil mask and on the demagnification factor of the BIGRE spaxel and the magnification of the reimaging optics. By this analysis, supersampling applies to the final exit slit function through Equation (22) as follows:

$$2 \cdot d_{pixel} \leq \left(\frac{D_{spaxel} \cdot m_{IFS}}{K \cdot S_{PM}} \right). \quad (60)$$

We can now study the effect of varying the pupil mask size on the slit function in terms of cross-talk performance and on the MTF in terms of aliasing.

Choosing a very large pupil mask, $S_{PM} \gg 1$, corresponds to transmitting the spaxel transmission profile without modification: its FWHM is D_{spaxel} and cross talk is zero. The MTF is a Jinc function with first zero at $1.22/s$, so sampling this slit with two pixels across its width causes aliasing of up to around 15%. On the other hand, choosing a very small pupil mask, $S_{PM} \ll 1$ creates a wide slit function with a shape approximately equal to an Airy pattern of $FWHM \sim D_{spaxel}/S_{PM}$. The cross talk is the same as that found for the TIGER case, and the MTF is equal to the classical MTF function for diffraction-limited optical systems. Sampling corresponding to half of the FWHM is exempt of any aliasing.

It is somewhat surprising to find in between these two extremes, the evolution of the FWHM is not monotonic, but passes through a minimum, located at $S_{PM} = 2.5$. At this position, the slit function has a Gaussian-like bell shape, and its FWHM is $\sim 0.56 \cdot D_{spaxel}$; see Figure 7. The slit function falls off rapidly, and its first secondary maximum peaks at values < 0.001 . Compared with the ones of an Airy function (> 0.01) this ensures a low level of cross talk. The spectral MTF also resembles a Gaussian function, with a monotonic fall-off; see Figure 8. For a sampling of two pixels across the FWHM, the aliasing is well below 6% (see Figure 8).

The presence of a minimum indicates that the size of the slit function could be stable with respect to variations in wavelength, indicating that the pupil mask works chromatically as a pupil

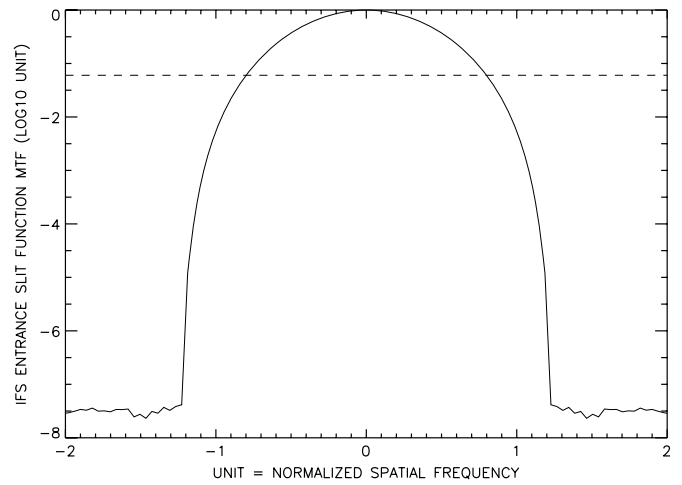


Figure 8. MTF of the BIGRE entrance slit. Filtering out the spatial frequencies above the one corresponding to the entrance slit FWHM (dashed horizontal line) produces a limited aliasing error: $MTF(s) | s > s_{FWHM} < 6\%$.

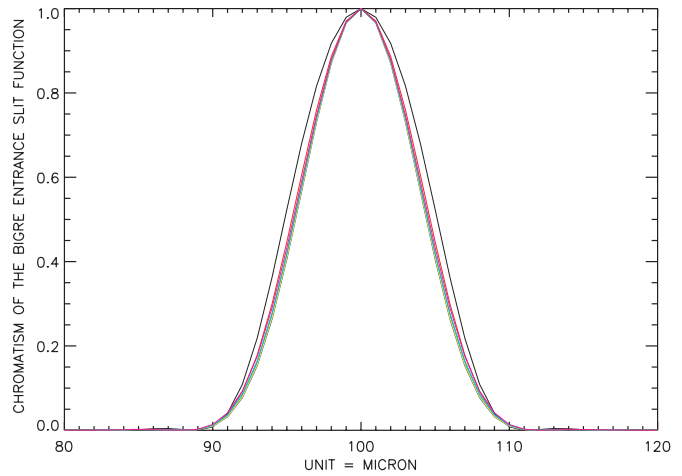


Figure 9. Normalized BIGRE entrance slit function. The example shows the case of the IFU optimized for SPHERE in the working wavelengths range: $0.95\text{--}1.35 \mu\text{m}$; colors indicate seven distinct wavelengths. (A color version of this figure is available in the online journal.)

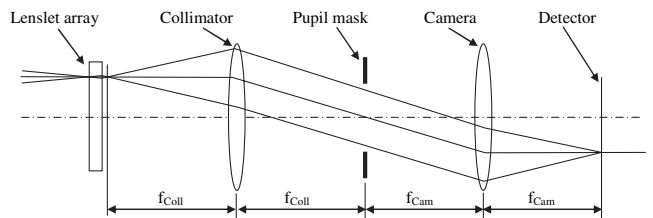


Figure 10. BIGRE spectrograph concept. The entrance slits plane is filled with the micro-images of the first surfaces of the BIGRE spaxels and the spatial filtering is done in the metapupil plane forming between collimator, having focal length f_{Coll} and the reimaging optics, having focal length $f_{Cam} \equiv m_{IFS} \cdot f_{Coll}$.

apodization (Jacquinot & Roisin-Dossier 1964). This is indeed the case, as indicated in Figure 9, where the slit function is plotted for several wavelengths in the range $0.95\text{--}1.35 \mu\text{m}$. We study the wavelength evolution of coherent and incoherent cross talks in Section 9.

This analysis suggests then that the spectrograph's entrance slit shape can be fixed selecting properly the pupil mask's

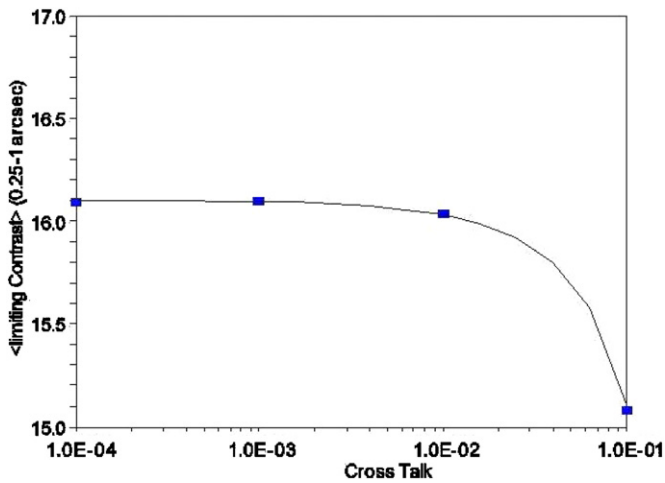


Figure 11. Average 5σ contrast over an azimuthal area comprised between 0.25 and 1 arcsec from a $J = 3.75$ (mag) star. The simulations are for 10^4 s exposure time and 90° field rotation. Filled squares are results of the IFS end-to-end simulations while the solid line represents the contrast curve expected by exploiting Equation (63) in order to obtain C_{pixel} via the S-SDI calibration technique. The adopted postcoronagraph contrast profile is the one presented by Boccaletti et al. (2008).

Table 2
Independent Parameters of a BIGRE-oriented IFS

Parameter	Symbol
Post-coronagraphic Pupil Size	$\equiv D$
IFS Cut-on Wavelength	$\equiv \lambda_{\text{min}}$
IFS Central Wavelength	$\equiv \lambda_c$
Size of the Single BIGRE Microlens	$\equiv D_{\text{spaxel}}$
Focal Length of the First BIGRE Optical Surface	$\equiv f_1$
Focal Length of the Second BIGRE Optical Surface	$\equiv f_2$
Size of the Pupil Mask in Unit of $\lambda_c \cdot F_1$	$\equiv S_{\text{MPM}}$
IFS Detector Pixel Size	$\equiv d_{\text{pixel}}$
IFS Optical Magnification	$\equiv m_{\text{IFS}}$
IFS Disperser (two-pixel) Resolving Power	$\equiv R$

minimum size. Once projected on the final detector plane, supersampling can be fixed by imposing that two pixels cover the spectrograph’s exit slit FWHM:

$$2 \cdot d_{\text{pixel}} \leq \left(\frac{m_{\text{IFS}}}{s_{\text{FWHM}}} \right), \tag{61}$$

where s_{FWHM} is the spatial frequency corresponding to a spatial period equal to the slit function FWHM, while according to Equation (26) hypersampling depends on the postcoronagraphic pupil size, the spectrograph’s working wavelengths range, and its resolving power.

Finally, as shown in Figure 10, the aim of the optics downstream the BIGRE lenslet array is to reimagine the entrance slit into the spectrograph’s image plane with the highest stability and optical quality; for this reason, the optical design can be fully dioptric. The requested stability is assured imposing the telecentricity of the entrance pupil. In turn, this implies that the metapupil forming between collimator and reimaging optics, which is the result of the overposition of individual micropupils forming inside the lenslet array, has a size equal to the size of a single micropupil, once properly magnified by the ratio between the equivalent focal length of the collimator optics and the focal length of the second optical surface of the single BIGRE lens, while the spatial filtering of the micropupils is obtained by adopting a unique pupil stop placed onto this spectrograph’s

metapupil plane with a physical size (D_{PS}) obtained as follows:

$$D_{\text{PS}} = D_{\text{MP}} \cdot \left(\frac{f_{\text{Coll}}}{f_2} \right), \tag{62}$$

where D_{MP} is fixed by Equation (56). Thus, a suitable dispersing device can be inserted in the optical train after this pupil stop allowing us to image the exit slits as true spectra on the spectrograph’s image plane.

9. BIGRE AND TIGER IFU SOLUTIONS FOR SPHERE IFS

Coherent and incoherent cross talks establish the actual imaging contrast measured onto the detector (C_{pixel}) with respect to the reference value (C_{spaxel}) depending on the spatial sampling of the postcoronagraphic speckle field. Their difference depends on cross talk just because the optical signal imaged by a fixed spaxel is spread over a number of detector pixels larger than the ones corresponding to it by geometrical optical propagation only, in a way which is proportional to the levels of cross talks. When the cross-talk coefficients are sufficiently small this difference can be approximated as

$$C_{\text{pixel}} - C_{\text{spaxel}} \approx -n \cdot (\text{CCT} + \text{ICT}), \tag{63}$$

where n is the number of adjacent spaxels around the fixed one, while CCT and ICT are the cross-talk coefficients defined by Equations (31) and (36), respectively.

For the IFS channel of SPHERE, the requested cross-talk coefficients have been determined through a series of simulations devoted to measure the contrast capabilities of this integral field spectrograph. The result is that the impact of cross talk is well reduced when the supersampling condition is verified. This fact can be explained heuristically remembering the meaning of the cross-talk errors over a fixed spectrograph’s exit slit: to replace its monochromatic intensity with the sum of this intensity and the average of the intensities proper to the exit slits corresponding to its adjacent spaxels (via the coherent cross-talk coefficient) together with the average of the intensities proper to the exit slits corresponding to its adjacent spectra (via the incoherent cross-talk coefficient). In the case of supersampling, adjacent exit slits do not suffer from a mutual shape variations, instead they suffer only from mutual differences in intensity due to the input postcoronagraphic speckle field. In this way, the residual between a fixed exit slit’s intensity and its ideal value (free from cross-talk errors) becomes small beyond a fixed threshold depending on the speckle rejection capabilities of the coronagraph. No gain in contrast is then possible for further decrements of the cross-talk coefficients. In the case of the IFS simulations this threshold returns to be 0.01 (see Figure 11). As a conclusion, the IFU solutions for the IFS of SPHERE should be compliant with this specification.

Figures 12 and 13 show the levels of incoherent cross talks, respectively, in the TIGER and BIGRE designs optimized for SPHERE, plotted against wavelength. While the incoherent cross talk is below the 1% threshold for both designs, the BIGRE design is clearly superior, showing a minimum towards the middle of the range corresponding to the wavelength at which the pupil mask is optimal. The coherent cross talk is greater than the incoherent one, as expected, but again the BIGRE design shows superior performance, and remains well below the 1% threshold across the spectral range of interest. The TIGER design, on the other hand, is not within the specified limit.

Table 3 resumes the solution we found for the BIGRE-oriented IFU of SPHERE allowing to reach the requested

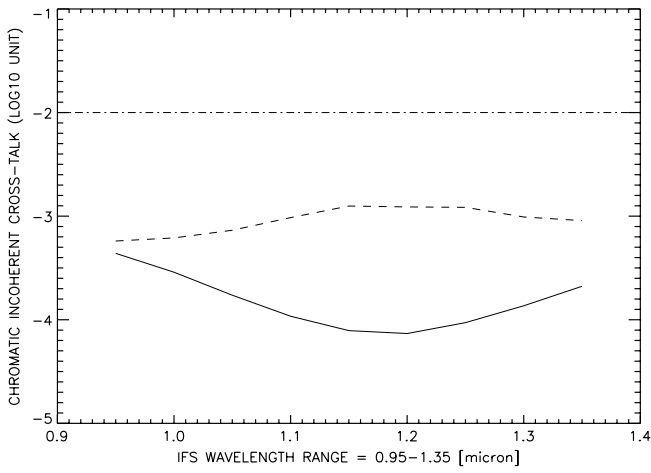


Figure 12. Incoherent cross-talk coefficient as a function of the wavelength in the range 0.95–1.35 μm . Solid line represents the BIGRE solution, dashed line the TIGER one and dot-dashed line the SPHERE IFS specification.

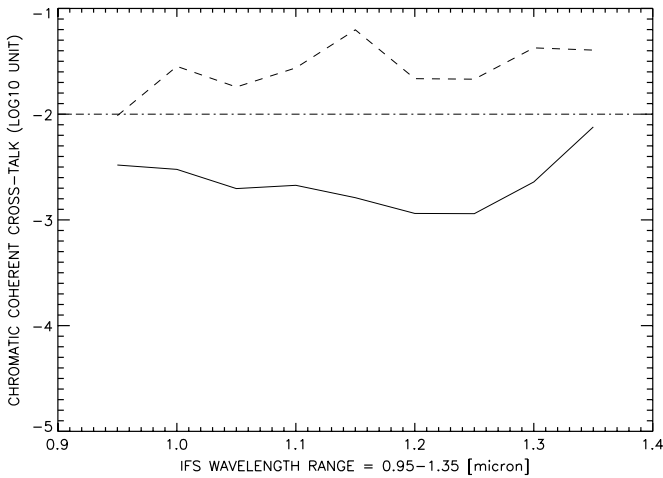


Figure 13. Coherent cross-talk coefficient as a function of the wavelength in the range 0.95–1.35 μm . Solid line represents the BIGRE solution, dashed line the TIGER one and dot-dashed line the SPHERE IFS specification.

Table 3

Basic Parameters Proper to the BIGRE Solution of SPHERE

$D_{\text{spaxel}} = 161.5 \mu\text{m}$	$\lambda_{\text{min}} = 0.95 \mu\text{m}$	$K = 4.1$	$F_{\text{out}} = 12$
$m_{\text{IFS}} = 1.69$	$d_{\text{pixel}} = 18 \mu\text{m}$	$R = 54$	

Table 4

Basic Parameters Proper to the TIGER Solution of SPHERE

$D_{\text{spaxel}} = 150 \mu\text{m}$	$\lambda_{\text{min}} = 0.95 \mu\text{m}$	$F_{\text{out}} = 7$
$m_{\text{IFS}} = 2.4$	$d_{\text{pixel}} = 18 \mu\text{m}$	$R = 24$

coherent and incoherent cross-talk levels. With this solution hypersampling is verified within the whole scientific field of view: the Nyquist radius is larger than the radial field of view imaged by the spectrograph’s optics (1.25 arcsec). Table 4 summarizes the solution we found for the TIGER-oriented IFU of SPHERE. This one allows us to reach the requested incoherent cross-talk limit but not the requested coherent cross-talk limit, while hypersampling is well verified as in the previous case.

Based on these results, a BIGRE design is chosen for the IFS channel of SPHERE, configured with circular spaxels in a hexagonal lattice configuration (see Figure 14).

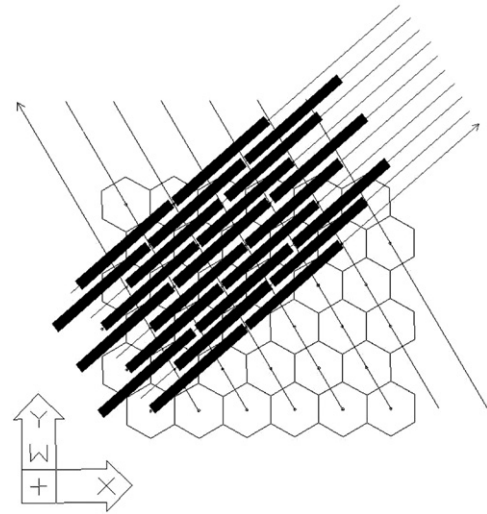


Figure 14. Sketch of the selected hexagonal configuration for the final spectra of SPHERE IFS. The left-oriented axis is the reference on the IFU plane (filled with hexagons representing a portion of the spaxels lattice), while the right-oriented axis traces the dispersion direction and the black rectangles the spectra imaged onto the detector plane. The spectra are 35 pixel long in the dispersion direction and the separation to the nearest neighborhood is 5 pixel, both in the spectral and in the spatial direction.

10. COMPARING DIFFERENT BIGRE AND TIGER SPAXEL SHAPES AND IFU LATTICE CONFIGURATIONS

In this Section we compare the slit functions generated through the TIGER and BIGRE image propagation, computed for different spaxel shapes and lattice configurations of the entire IFU. This comparison is made assuming common spaxel size and wavelength. This analysis allows us to derive the best lenslet-array optical concept and the optimum IFU lattice configuration in the ideal diffraction limited case, i.e., when the object plane of the lenslet array is an unresolved entrance pupil.

The diagnostic quantities exploited for this analysis are the amount of coherent and incoherent intensities both measured onto the entrance slits plane of the spectrograph, before any chromatical dispersion and reimaging onto a suited detector plane. To this aim, it is important to stress the meaning of coherent and incoherent signals and the one of their related cross-talk terms. Coherent signal is the intensity term due to interference between adjacent spaxels measured at any point of the entrance slits plane. Such a signal depends on the optical path difference between adjacent spaxels only; in this sense spaxels can be compared to apertures of a standard grating. The coherent cross-talk coefficient is the maximum amount of coherent signal, see Section 6.1. Incoherent signal is the stray intensity terms due to the image propagation diffraction effects measured at any point of the entrance slits plane. Such a signal depends on the distance between adjacent spectra projected onto this plane; in this sense this signal depends on the final configuration of the spectra on to the detector plane. The incoherent cross-talk coefficient is the maximum amount of incoherent signal, see Section 6.2.

The comparison between TIGER and BIGRE is performed for two distinct shapes of the single spaxel (circular and square) and for two distinct IFU lattice configurations (hexagonal and square). The combination of such different shapes and configurations allows us to compare the TIGER and the BIGRE concepts in term of coherent and incoherent signals for standard lenslet-array optical setups. It is important to note that these simulations consider as input a normalized signal without

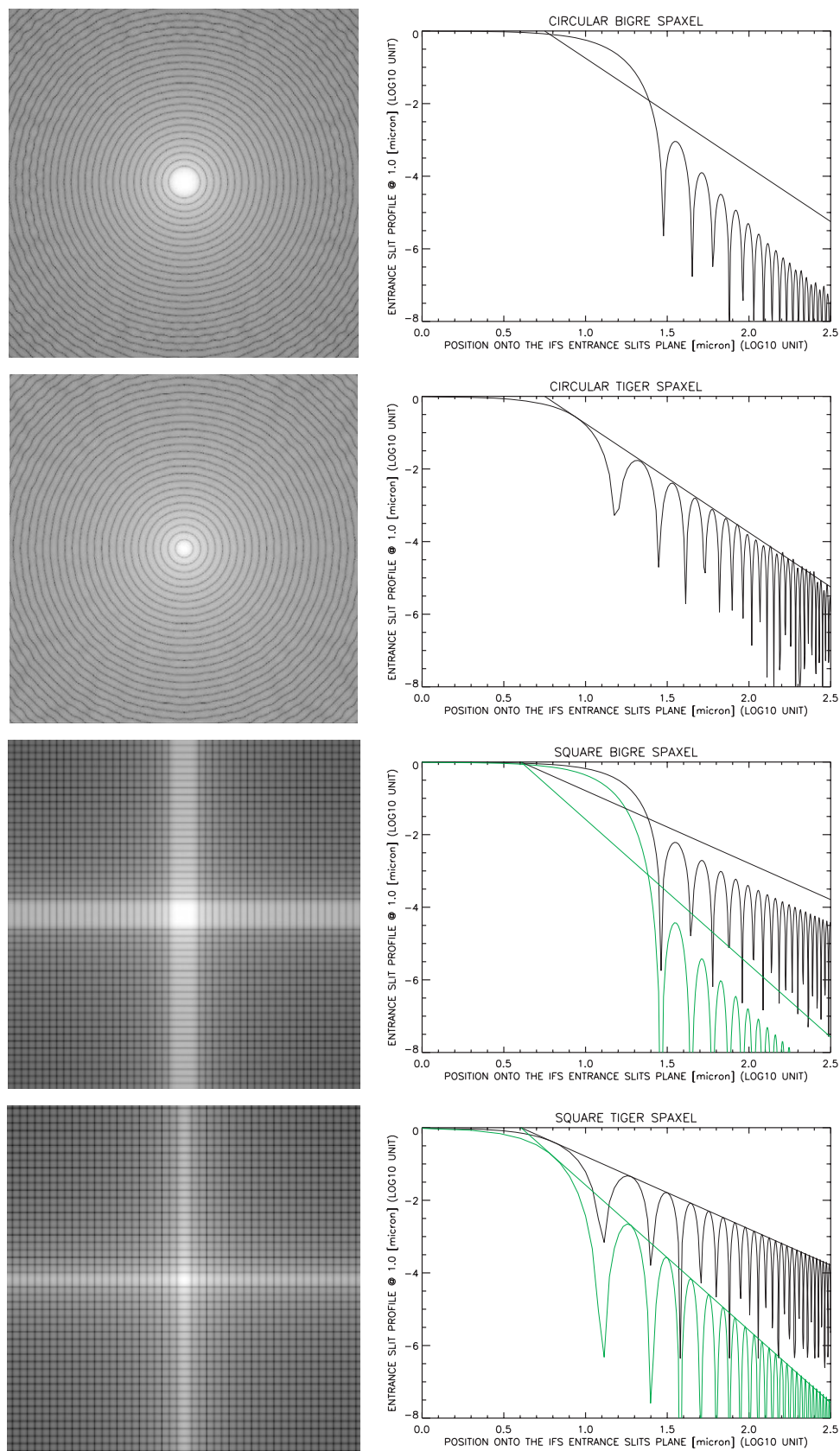


Figure 15. Normalized BIGRE and TIGER slit functions comparison. The adopted lenslet aperture is always $161.5 \mu\text{m}$, i.e., the one proper to the BIGRE solution for SPHERE (see Table 2); the adopted wavelength is always $1 \mu\text{m}$. First column shows the images given by individual spaxels in a bilogarithmic scale. Second column shows the relative profiles (in the case of square spaxel shape diagonal profiles are presented in green color). The power laws fitting the slit functions proper to a circular and a square TIGER-oriented spaxel are indicated for reference by solid lines. These simulations consider Fraunhofer propagation only and assume as input signal of the lenslet array an unresolved entrance pupil. Finally, results are independent to the detector pixel scale just because images refer to the spectrograph's entrance slits plane.

(A color version of this figure is available in the online journal.)

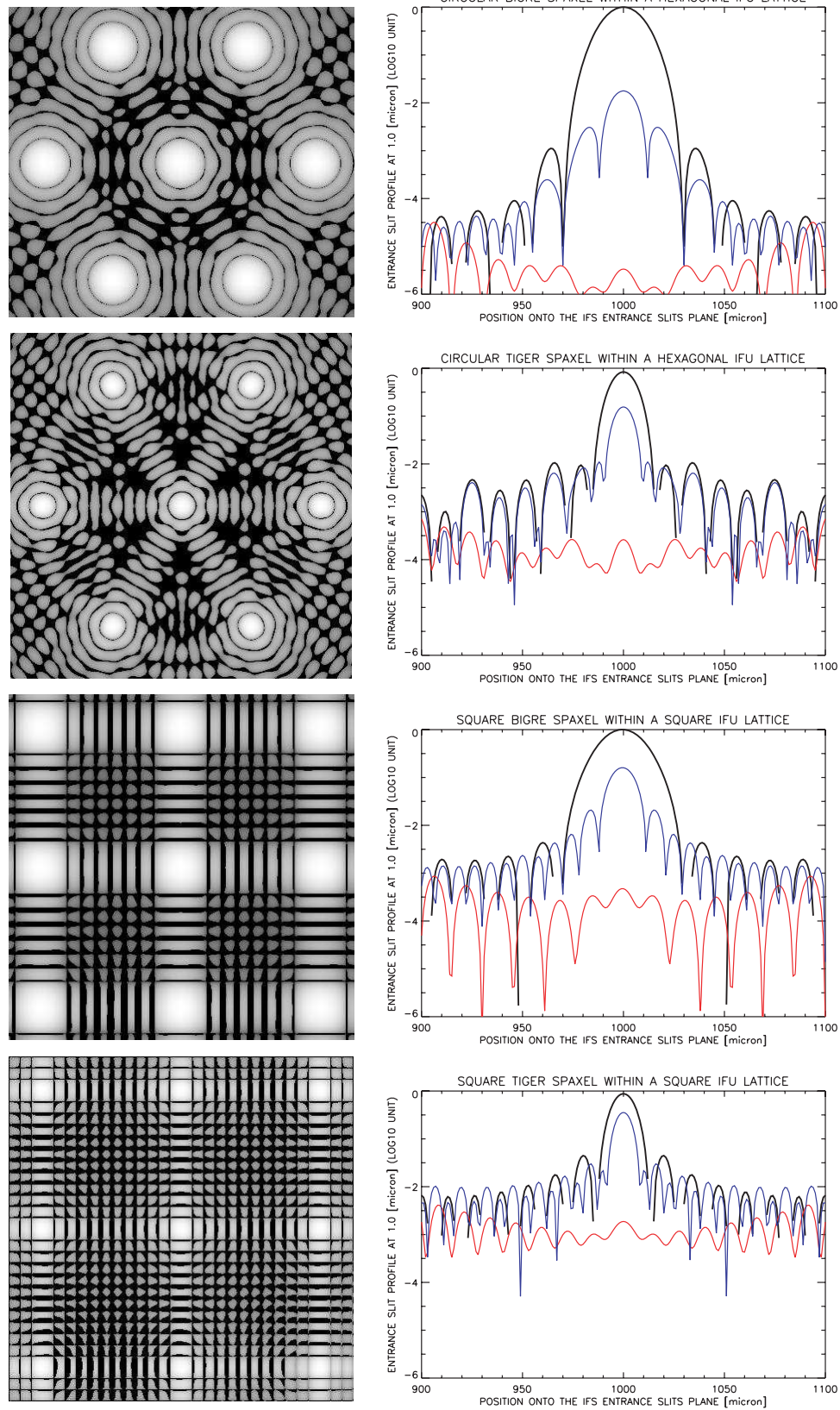


Figure 16. Normalized BIGRE and TIGER slit functions comparison. The adopted lenslet aperture is always $161.5 \mu\text{m}$, i.e., the one proper to the BIGRE solution for SPHERE (see Table 2); the adopted wavelength is always $1 \mu\text{m}$. First column shows the images given by an individual spaxel together with its adjacent ones and for different IFU lattice configurations. Second column shows the relative profiles: black color indicates the slit function (the signal represents the detection expected if only the central spaxel were illuminated); red color indicates the signal due to adjacent spaxels only; blue color is the coherent signal arising from the interference of the signal proper to the central spaxel with all the adjacent ones. These simulations consider Fraunhofer propagation only and assume as input signal of the lenslet array an unresolved entrance pupil. Finally, results are independent to the detector pixel scale just because images refer to the spectrograph's entrance slits plane.

(A color version of this figure is available in the online journal.)

amplitude and phase differences between adjacent spaxels. In this way, the results obtained are independent with respect to the actual speckle pattern beating the IFU.

As Figure 15 indicates, adopting a bilogarithmic scale, the single BIGRE slit gets an intensity profile steeper than the one proper to the single TIGER slit both in the case of circular and square shapes. More in detail, the upper envelope to the slit intensity profile proper to a circular TIGER-oriented spaxel is a power law with index equal to -3 , while the same quantity for a square TIGER-oriented spaxel is a power law with index equal to -2 along the aperture side and with index equal to -4 along its diagonal. At contrary, the upper envelope of the slit intensity profile proper to a circular BIGRE-oriented spaxel is not a power law (only its asymptotic tail is fitted quite well with a power law having index $\propto -4.5$); the same quantity is not a power law in the case of a square BIGRE-oriented spaxel too (only its asymptotic tail is fitted quite well with a power law with index $\propto -3$ in the direction of the aperture side and index $\propto -6$ along its diagonal).

The result is that the BIGRE-oriented circular aperture within a hexagonal lattice configuration allows a superior suppression of coherent and incoherent signals, while the slits generated by a circular TIGER-oriented aperture in a hexagonal lattice are similar—in this context—to the ones generated by a square BIGRE-oriented aperture in a square lattice. Finally, the slits generated by a square TIGER-oriented aperture in a square lattice are the worst in term of coherent and incoherent signals suppression, see Figure 16. Hence, the contribution of nonadjacent spaxels can be neglected when evaluating the cross-talk signals in the case of a BIGRE spectrograph, just because the power laws fitting—in a bilogarithmic plot—the intensity distribution proper to the TIGER slit functions do not fit at all the one proper to the BIGRE slit functions. At contrary, the intensity distribution proper to the BIGRE slit functions can be only approximated with lower index power laws. Thus, what for a TIGER lenslet array represents an estimate only, for a BIGRE lenslet array it gives realistic measures of the signals due to the spectrograph's slit functions cross-talk.

11. CONCLUSIONS

By integral field spectroscopy it is possible to realize the S-SDI calibration technique in the way proposed by Berton et al. (2006), and—at least in a few cases—to get the spectrum of candidate extrasolar giant planets adopting suited spectral de-convolution recipes, as the one proposed by Thatte et al. (2007). However, these techniques can increase the contrast performances only when several sampling conditions, both in the spatial and in the spectral domain of the speckle field, are verified.

Our effort has been then to discuss in general terms the critical sampling conditions needed to deal with a speckle field data cube before applying on it the S-SDI calibration technique or any spectral de-convolution recipe.

To this purpose, we evaluated the impact of the cross talk as a function of various parameters of a lenslet-based integral field spectrograph, especially in the case of trying to minimize the number detector pixels (which is an issue in general for IFS) in the case of strong specifications, as the ones requested for high-contrast imaging. For this reason we conceived a new optical scheme—we named BIGRE—and characterized it in the specific case of the IFS channel foreseen inside SPHERE, showing that a BIGRE-oriented spectrograph is conceptually feasible by standard dioptric optical devices. Once applied to

the technical specifications of this instrument, a BIGRE integral field unit is able to take into account the effects appearing if a lenslet array is used in diffraction-limited conditions. Specifically, we proved here that coherent and incoherent cross-talk coefficients reach values deeper than for a TIGER IFU when applied to the same optical frame. More in general, the comparison between the BIGRE and the TIGER spaxel concept has been pursued in terms of coherent and incoherent cross-talk suppression, adopting a common size for the single aperture and a fixed monochromatic wavelength for the wavefront propagation. In the ideal case of uniform illumination with unresolved entrance pupil, the circular BIGRE spaxel within an hexagonal IFU lattice configuration shows to be the optimal solution among the ones we investigated.

The authors thank Roberto Ragazzoni for the support he gave them in the development of this subject, from the primeval CHEOPS project to SPHERE. Jacopo Antichi thanks personally Bernard Delabre for a dedicated work session at ESO-Garching in 2007 April, devoted to the final design optimization of the BIGRE-oriented spectrograph to be mounted in SPHERE and Christophe Vérinaud for his advising during the completion of the manuscript. Jacopo Antichi is supported by LAOG through the European Seventh Framework Programme INFRA-2007-2.2.1.28.

REFERENCES

- Bacon, R., et al. 1995, *A&AS*, **113**, 347
 Bacon, R., et al. 2001, *MNRAS*, **326**, 23
 Baraffe, I., Chabrier, G., Allard, F., & Hauschildt, P. H. 2002, *A&A*, **382**, 563
 Berton, A., Gratton, R. G., Feldt, M., Henning, T., Desidera, S., Turatto, M., Schimid, H. M., & Waters, R. 2006, *PASP*, **118**, 1144
 Beuzit, J.-L., et al. 2008, *Proc. SPIE*, **7014**, 701418
 Biller, B. A., Close, L., Lenzen, R., Brandner, W., McCarthy, D. W., Nielsen, E., & Hartung, M. 2004, *Proc. SPIE*, **5490**, 389
 Boccaletti, A., Carbillet, M., Fusco, T., Mouillet, D., Langlois, M., Moutou, C., & Dohlen, K. 2008, *Proc. SPIE*, **7015**, 70156E
 Born, M., & Wolf, E. 1965, *Principles of Optics. Electromagnetic Theory of Propagation, Interference and Diffraction of Light* (3rd ed., Oxford: Pergamon)
 Burrows, A., Sudarsky, D., & Hubeny, I. 2004, *ApJ*, **609**, 407
 Burrows, A., Sudarsky, D., & Lunine, J. I. 2003, *ApJ*, **596**, 587
 Cavarroc, C., Boccaletti, A., Baudoz, P., Fusco, T., & Rouan, D. 2006, *A&A*, **447**, 397
 Chauvin, G., Lagrange, A.-M., Dumas, C., Zuckerman, B., Mouillet, D., Song, I., Beuzit, J.-L., & Lowrance, P. 2004, *A&A*, **425**, L29
 Chauvin, G., et al. 2005, *A&A*, **438**, L29
 Dohlen, K., et al. 2006, *Proc. SPIE*, **6269**, 62690Q
 Gisler, D., et al. 2004, *Proc. SPIE*, **5492**, 463
 Goodman, J. W. 1996, *Introduction to Fourier Optics* (2nd ed., New York: McGraw-Hill)
 Jacquinet, P., & Roisin-Dossier, B. 1964, *Prog. Opt.*, **3**, 29
 Lafrenière, D., Jayawardhana, R., & van Kerkwijk, M. H. 2008, *ApJ*, **689**, L153
 Lagrange, A.-M., et al. 2008, *A&A Lett*, in press
 Lenzen, R., Close, L., Brandner, W., Hartung, M., & Biller, B. 2005, *Science with Adaptive Optics* (Berlin: Springer)
 Kalas, P., et al. 2008, *Science*, **322**, 1345
 Kasper, M. E., et al. 2008, *Proc. SPIE*, **7015**, 701515
 Maréchal, A. 1947, *Rev d'Opt.*, **26**, 257
 Macintosh, B., Poyneer, L., Sivaramakrishnan, A., & Marois, C. 2005, *Proc. SPIE*, **5903**, 59030J
 Macintosh, B.-A., et al. 2008, *Proc. SPIE*, **7015**, 701518
 Marois, C., Doyon, R., & Nadeau, D. 2000, *PASP*, **112**, 91
 Marois, C., Doyon, R., Nadeau, D., Racine, R., Riopel, M., Vallée, P., & Lafrenière, D. 2005, *PASP*, **117**, 745
 Marois, C., Phillion, D. W., & Macintosh, B. 2006, *Proc. SPIE*, **6269**, 62693M
 Marois, C., Lafrenière, D., Macintosh, B., & Doyon, R. 2008a, *ApJ*, **673**, 647
 Marois, C., Macintosh, B., Barman, T., Zuckerman, B., Song, I., Patience, J., Lafrenière, D., & Doyon, R. 2008b, *Science*, **322**, 1348

- Neuhaeuser, R., Guenther, E., Wuchterl, G., Mugrauer, M., Beladov, A., & Hauschildt, P.-H. 2005, *A&A*, **435**, L13
- Perrin, D. P., Sivaramakrishnan, A., Makindon, R. B., Oppenheimer, B. R., & Graham, J. R. 2003, *ApJ*, **596**, 702
- Prieto, E., & Vivès, S. 2006, *New Astron. Rev.*, **50**, 279
- Pyoneer, L. A., & Macintosh, B. 2004, *J. Opt. Soc. Am. A*, **21**, 810
- Racine, R., Walker, G. A. H., Nadeau, D., Doyon, R., & Marois, C. 1999, *PASP*, **111**, 587
- Ren, D., & Wang, H. 2006, *ApJ*, **640**, 530
- Smith, W. H. 1987, *PASP*, **99**, 1344
- Sparks, W. B., & Ford, H. C. 2002, *ApJ*, **578**, 543
- Sudarsky, D., Burrows, A., & Pinto, P. 2000, *ApJ*, **538**, 885
- Sudarsky, D., Burrows, A., & Hubeny, I. 2003, *ApJ*, **588**, 1121
- Thatte, N., Abuter, R., Tecza, M., Nielsen, E. L., Clarke, F. J., & Close, L. M. 2007, *MNRAS*, **378**, 1229
- Vérinaud, C., et al. 2008, *Proc. SPIE*, 7014, 70141J